

# Acoustic pulse propagation near a right-angle wall

Lanbo Liu<sup>a)</sup>

USA ERDC Cold Regions Research and Engineering Laboratory, 72 Lyme Road,  
Hanover, New Hampshire 03755-1290 and  
Department of Civil and Environmental Engineering, University of Connecticut, 261 Glenbrook Road,  
U-2037, Storrs, Connecticut 06269-2037

Donald G. Albert<sup>b)</sup>

USA ERDC Cold Regions Research and Engineering Laboratory, 72 Lyme Road, Hanover,  
New Hampshire 03755-1290

(Received 14 July 2005; revised 3 February 2006; accepted 6 February 2006)

Experimental measurements were conducted around a right-angle wall to investigate the effect of this obstacle on sound propagation outdoors. Using small explosions as the source of the acoustic waves allowed reflected and diffracted arrivals to be discerned and investigated in detail. The measurements confirm that diffraction acts as a low-pass filter on acoustic waveforms in agreement with simple diffraction theory, reducing the peak pressure and broadening the waveform shape received by a sensor in the shadow zone. In addition, sensors mounted directly on the wall registered pressure doubling for nongrazing angles of incidence in line-of-sight conditions. A fast two-dimensional finite difference time domain (FDTD) model was developed and provided additional insight into the propagation around the wall. Calculated waveforms show good agreement with the measured waveforms. © 2006 Acoustical Society of America. [DOI: 10.1121/1.2180530]

PACS number(s): 43.28.En, 43.28.Js, 43.20.El, 43.50.Vt [LCS]

Pages: 2073–2083

## I. INTRODUCTION

Sound propagation in an urban environment is currently an active research topic in both civil and military applications. Understanding acoustic propagation in this environment is important for noise reduction and for designing and predicting the performance of various sensor systems. The presence of buildings in an urban environment introduces reflections, diffractions, and multiple propagation paths that are not present in simpler situations. As the foundation for studying the effects of multiple buildings, which is the theme for a future paper, the perturbations caused by the presence of a single obstacle are the focus of this study.

The effect of barriers on acoustic propagation has been studied extensively, especially to reduce traffic noise. Ray theory treatments are often discussed in textbooks (e.g., Refs. 1 and 2) and Pierce<sup>3,4</sup> has developed a theoretical treatment that is often used in such applications. In recent years the boundary element method<sup>5–7</sup> has proved useful for solving many of these problems, and a number of analytical or semianalytical methods have been developed to investigate the urban environment and street canyons (e.g., Refs. 8–10).

In part because of the nature of traffic noise, most previous experimental work has focused on the frequency domain, and acoustic pulses have only occasionally been used in the past to investigate simple barriers.<sup>11–16</sup> Nonplanar obstacles are not often treated, although Pierce (Ref. 4, p. 498) discusses a single-frequency calculation for propagation around a building corner.

To examine the nature and properties of various waves involved in the interaction with an obstacle, experimental measurements were conducted outdoors on a full-scale, right-angle wall using impulsive sources. A concrete block wall was constructed in an open field and instrumented with pressure sensors. Small explosive charges were detonated at various locations near the wall and the resulting pressure waveforms were recorded using a digital seismograph. These measurements investigated both line-of-sight (LOS) and non-line-of-sight (NLOS) situations.

In recent years, the finite-difference time domain (FDTD) method has gained popularity in simulating different wave propagation phenomena (e.g., Refs. 17–19). Here, the two-dimensional FDTD method is applied to model the experimental measurements on a personal computer. Some of the advantages of the finite-difference method are the ability to include a variety of acoustic pulses, complex barrier or building geometries, and spatially varying sound speeds. In addition, viewing the computational results in an animated movie format can provide insight to complex wave propagation phenomena arising from the interaction of the waves with obstacles. This paper demonstrates that the FDTD technique is a useful tool to understand sound propagation physics in a complex environment.

The next section discusses experimental measurements that were made on an isolated concrete block wall to investigate the simplest case of building effects, reflection, and diffraction. Next, a two-dimensional finite-difference time domain prediction method is developed and validated by comparison with the experimentally measured waveforms. This method is shown to be an accurate tool for the study of outdoor sound propagation in complex situations.

<sup>a)</sup>Electronic mail: lanbo.liu@erdc.usace.army.mil

<sup>b)</sup>Electronic mail: donald.g.albert@erdc.usace.army.mil

TABLE I. Geometry of the measurements. Grid coordinates in meters of walls, sensors, and source locations corresponding to Fig. 1.

Sensor	X	Y	Z	Description	Line-of-sight (LOS)
	-9.4	0.0		Left end of front wall	
A	-4.6	6.0	0.0	Near front wall	All source locations
B	-4.6	3.0	1.5	Near front wall	All source locations
C	-4.6	1.5	1.5	Near front wall	All source locations
D	-4.6	0.0	1.5	On front wall	All source locations
	0.0	0.0		Corner of both walls	
E	0.0	-6.0	1.5	On side wall	S5
F	1.5	-6.0	1.5	Near side wall	S4-S5
G	3.0	-6.0	1.5	Near side wall	S4-S5
H	6.0	-6.0	1.5	Near side wall	S3-S5
	0.0	-9.4		Lower end of side wall	
I	-4.6	-0.2	1.5	Behind the front wall	S1
J	-4.6	-3.0	0.0	Behind the front wall	S1
K	-4.6	-30.0	0.0	30 m behind front wall	S1-S3, S5
SP1	-34.6	0.0	1.5	Source parallel with front wall	
SP2	-30.6	15.0	1.5	Source 30° from front wall	
SP3	-19.6	26.0	1.5	Source 60° from front wall	
SP4	-4.6	30.0	1.5	Source perpendicular to front wall	
SP5	10.4	26.0	1.5	Source 60° from front wall	

## II. EXPERIMENTAL MEASUREMENTS

For the experimental measurements, a right-angle wall with equal sides, each 9.4 m long and 3.5 m high, was constructed in an open field using concrete blocks. Pressure sensors were installed on and near the walls (most at a height of 1.5 m above ground level, see Table I), and 0.28-kg charges of C4 explosive, 1.5 m above ground level, were detonated at various locations 30 m from the center of the front wall (see Fig. 1). The resulting pressure pulses were recorded us-

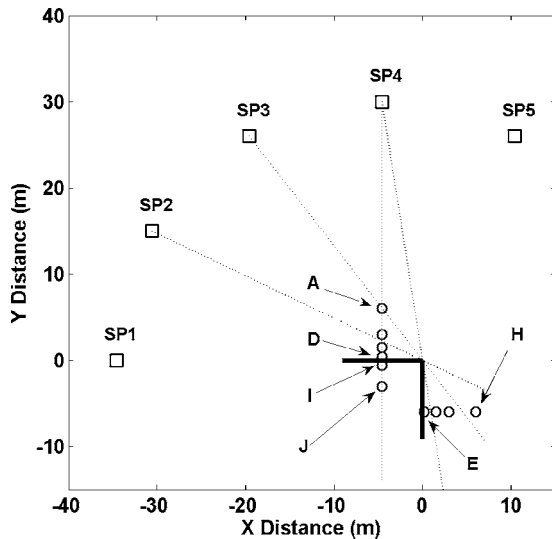


FIG. 1. Plan view of the experimental geometry used for the wall measurements. The horizontal wall segment along the  $x$  axis is referred to as the front wall, and the vertical wall segment parallel to the  $y$  axis is called the side wall. Circles indicate the location of pressure sensors and squares the source locations. Dotted lines indicate line-of-sight (LOS) ray paths. A sensor located at  $(-4.6, -30)$  is omitted from the plot. The coordinates of all of the sources, sensors, and walls are given in Table I.

ing a Bison Model 9048 digital seismograph at a sampling rate of 5 kHz and with a response bandwidth of 3–2500 Hz. This experimental geometry allowed the reflection and diffraction of the low-amplitude blast waves by the right-angle wall to be studied in detail.

The measured pressure waveforms for sensors located near the center of the front and side walls for all of the source positions are shown in Fig. 2. In this figure, the top four waveforms are for sensors A–D near the front wall, while the lower four waveforms are for sensors E–H near the side wall. These measured waveforms reveal a number of characteristics of acoustic pulse interaction with the walls.

The front wall sensors A–D are all within the “line-of-sight” (LOS) of the source positions and have a direct wave arrival in every case. Examining the waveforms in Fig. 2 for these front wall sensors for source position 1 (SP 1) shows that grazing incidence does not have a visible effect on the sensor waveforms. All the waveforms are nearly the same in appearance and have about the same peak pressure amplitude. The positive pulse duration is typically around 5 ms, roughly indicating a peak frequency of about 100 Hz and a wavelength of about 3.5 m. The waveform for sensor A, farthest from the front wall (the top row in Fig. 2), looks slightly different from the others. These differences might occur because this sensor is at ground level, while the other sensors B–D are located 1.5 m above ground level.

At all of the other source positions, reflected waves are visible in the sensors located some distance from the front wall. The interference of the reflected wave with the direct wave depends on the geometry and travel time of the reflected wave. In all cases, the peak pressure of the reflected wave is smaller than the direct wave. The amplitudes of the direct and reflected waves at normal incidence lead to an

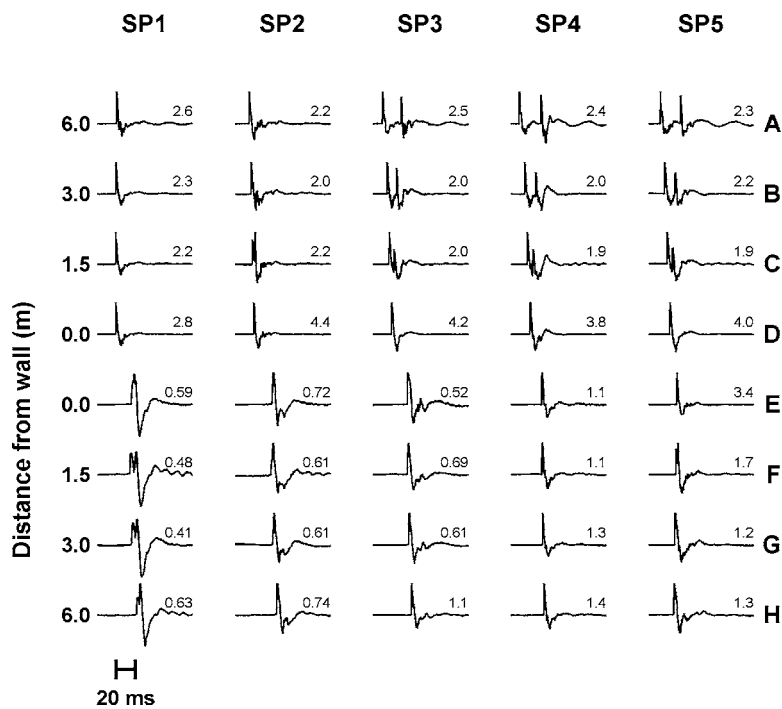


FIG. 2. Normalized pressure waveforms measured for the geometry shown in Fig. 1. Each column contains waveforms recorded for a particular source point and is 100 ms in duration. In each column, the top four waveforms are for sensors A–D located 6, 3, 1.5, and 0 m away from the front wall. The next four waveforms were recorded by sensors E–H located 0, 1.5, 3, and 6 m from the side wall. Each waveform is 100 ms in duration and labeled with the peak absolute pressure in kPa. See Fig. 1 and Table I for the experimental geometry.

estimate for the reflection coefficient of the wall as approximately 0.93. The high value of the reflection coefficient indicates that the finite size of the wall has little effect on the reflected energy.

All of the sensors located near the side wall (sensors E–H) are in the shadow zone for source positions 1 and 2, and some remain in the shadow for source positions 3 (sensors E–G at 0, 1.5, and 3 m) and 4 (sensor E at 0 m). For all of the non-line-of-sight (NLOS) sensors at source positions 1–3, the peak pressure amplitude drops from about 2.2 kPa to about 0.6 kPa, a reduction by a factor of nearly 4. When a sensor is near the shadow boundary, the peak pressure is reduced by about a factor of 2 to about 1.1 kPa. In addition, the NLOS waveforms have longer time durations and broader pulse widths than the LOS waveforms, with the positive duration typically increasing from 5 ms to 6–8 ms. For nongrazing LOS conditions, the wall-mounted sensors have approximately twice the peak pressure of the nearby sensors that are not on the wall. This “pressure doubling” is caused by the constructive interference of the direct and reflected waves.

Figure 3 compares a LOS sensor waveform with a NLOS sensor waveform, recorded with the source at SP1. The LOS sensor B was located 3 m from the front wall and the NLOS sensor E was located 0 m from the side wall. The LOS waveform is identical to waveforms measured in an open field, with no visible effect from the front wall. The direct wave has peak positive and negative pressures of 2300 and 890 Pa, respectively. For the NLOS sensor, three different diffracted arrivals are possible: a ray around the right-angle corner, a ray over the top of the wall, and a ray around the lower end of the side wall (see Fig. 1). All of these rays should arrive within a few ms of each other, and the small fluctuations near the peak pressure of the waveform indicate that interference is occurring.

Comparison of the pressure waveforms in Fig. 3 shows clearly that the diffracted waveform is a low-pass filtered version of the line-of-sight waveform. The peak pressure in the shadow zone is reduced by a factor of about 3 above

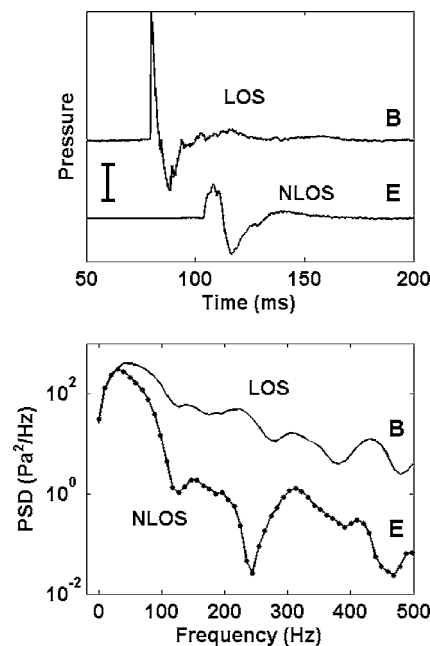


FIG. 3. Measurements illustrating the low-pass filtering effect of diffraction around a corner. The source of the waves was located at SP1 in Fig. 1. The positions of the line-of-sight (LOS) sensor B, 3 m in front of the front wall, and the non-line-of-sight (NLOS) sensor E, mounted on the side wall, are shown in Fig. 1. (Top) Pressure waveforms. The vertical bar indicates 1 kPa, and the measured peak positive pressures were 2300 for the LOS waveform and 590 Pa for the NLOS waveform. For the LOS wave, the positive duration was 4.0 ms and the entire waveform duration was 20.6 ms, while the durations increased to 9.4 and 29.1 ms for the NLOS wave. (Bottom) Power spectral densities of the two waveforms. The NLOS waveform has far less high-frequency content compared to the LOS waveform.

geometrical spreading, and the signal duration is longer. Both of these changes are typical time domain characteristics of low-pass filtering. The spectra calculated from these waveforms (also presented in Fig. 3) show that frequency components of 100 Hz and higher are reduced by two orders of magnitude in the shadow while the lower frequency content is not changed. This low-pass filtering effect is visible in previous higher frequency measurements<sup>11,12</sup> and agrees with insertion loss predictions from simple barrier diffraction theories (e.g. Refs. 1 and 4).

### III. FINITE-DIFFERENCE TIME DOMAIN NUMERICAL MODELING

Because barriers are often used in practical situations to reduce traffic or industrial noise, theoretical methods of predicting barrier effects using continuous wave or single-frequency sources have received a great deal of attention. However, these methods may predict constructive or destructive interference for waves with different propagation distances that does not occur when pulses are used instead of continuous sources. In addition, these methods are often limited to simplified geometries. The finite-difference method, a numerical method that overcomes these limitations, is used for the calculations presented here.

#### A. The finite-difference method

The finite-difference method is an important computational tool that has been used on many different wave propagation problems, including electromagnetics,<sup>20</sup> seismology,<sup>21</sup> and underwater acoustics.<sup>22</sup> In this section the general characteristics of the method are discussed and applied to outdoor sound propagation in the following sections. The basic method is to divide the spatial domain into a discrete grid of nodes and approximate the derivatives appearing in the equations of motion using finite differences between adjacent grid values. Similarly, the time variable is also divided into discrete steps and evaluated using finite differences. This method is commonly called the finite-difference time domain (FDTD) method.

In this case the acoustic propagation is expressed as a set of first-order, velocity-pressure coupled differential equations, similar to the motion and continuity expressions.<sup>23,24</sup> In a two-dimensional  $(x,y)$  plane, these equations can be expressed as

$$\begin{aligned}\frac{\partial p}{\partial x} &= -\rho \frac{\partial u}{\partial t}, \\ \frac{\partial p}{\partial y} &= -\rho \frac{\partial v}{\partial t}, \\ \frac{\partial u}{\partial x} + \frac{\partial v}{\partial y} &= -\frac{1}{\rho c^2} \frac{\partial p}{\partial t},\end{aligned}\quad (1)$$

where  $u$  and  $v$  are the  $x$  and  $y$  components of the particle velocity,  $p$  is the pressure,  $\rho$  is the density, and  $c$  is the sound speed of the medium. [These are Eqs. (1)–(3) of Ref. 24.] For a spatial grid size of  $h$ , the first-order spatial partial de-

derivatives appearing in the above equations can be approximated by

$$\left. \frac{\partial u}{\partial x} \right|_{t=n\Delta t} \approx \frac{1}{2h} [u(i+1,j;n) - u(i-1,j;n)] \quad (2)$$

with similar approximations for the  $y$  and  $t$  derivatives. In the above equation,  $u(i,j;n)$  represents the  $x$  component of the particle velocity at  $(x,y)$  grid point  $(i,j)$  and at time step  $n$ . Using these approximations the equations of motion can be rewritten in finite-difference form (see the Appendix).

There are two steps to determine the size of the grid and the length of the time step to insure numerical stability when implementing the FDTD algorithm. First, for a second-order finite difference, as adapted in this study, 20 spatial nodes per major wavelength are needed to suppress unwanted numerical dispersion. Next, for a given grid size  $h$ , the time step must meet the theoretical Courant stability criterion<sup>24</sup>

$$\Delta t \leq h/(c\sqrt{2}) \quad (3)$$

for the two-dimensional case. (In three-dimensional cases the square root of 2 is replaced by the square root of 3 in the denominator.) However, for problems involving materials having a high impedance contrast, the Courant condition of Eq. (3) may not be sufficient to insure numerical stability. A more stringent stability criterion with a much smaller time step has been imposed on the calculations in this paper of

$$\Delta t = h/(16c) \quad (4)$$

and is discussed further below.

The finite-difference equations are solved using a staggered difference algorithm proposed by Yee<sup>20</sup> in a two-dimensional spatial domain (see the Appendix). The computations are also staggered between the air pressure  $p$  and the particle velocity  $v$  in the time domain. Yee's staggered grid algorithm remains the most economical and robust way to carry out finite-difference time domain calculations.<sup>19</sup>

The perfectly matched layer (PML) technique<sup>25</sup> was adapted for the absorption boundary condition and achieved highly effective suppression of reflections from the domain boundaries. Numerical experiments demonstrated that an eight-layer PML boundary condition reduced the reflected error by 30–40 dB over any previously proposed absorption boundary conditions.<sup>17</sup> This method has also been successfully implemented in modeling seismic waves<sup>26</sup> and radar waves.<sup>27</sup>

#### B. Two-dimensional approximation

While the solution of the finite-difference equations discussed in the previous section is straightforward, a very fine spatial grid is required for an accurate solution as discussed below. This requirement normally limits finite-difference calculations for outdoor sound propagation problems to supercomputers or specialized multiprocessor networks. To reduce the computational effort and make the problem tractable on a desktop computer, a simplified two-dimensional model is used to represent the real three-dimensional world. This reduction of the calculations to two dimensions has substantial benefits but also introduces a number of approximations and

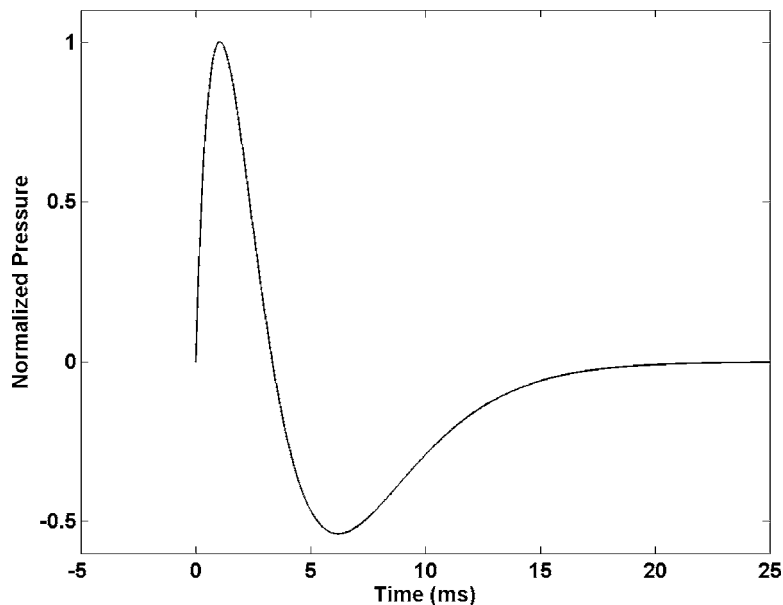


FIG. 4. The source pulse used in the finite-difference calculations. This pulse waveform was calculated from Eq. (5) with the parameter values of  $f=150$  Hz,  $a=16$ ,  $b=\frac{1}{4}$ , and  $c=\frac{1}{3}$ .

limitations to the modeling capability. While the kinematics of the computations (e.g., the speed and shape of the wavefronts and the arrival times) remain accurate, the dynamics (pressure amplitudes) differ from the three-dimensional situation and must be corrected if the calculations are to be compared to real measurements.

In the real physical world and in actual measurements, a point source generates a spherical acoustic wave with a geometric spreading factor of  $1/ct=1/r$ . However, the two-dimensional model uses a line source, which extends to infinity in the direction perpendicular to the model plane. This source generates a cylindrical wave with the geometric spreading of  $1/\sqrt{ct}=1/\sqrt{r}$ . Thus the two-dimensional modeling results are renormalized by an additional factor of  $1/\sqrt{r}$  to account for the actual three-dimensional geometric spreading present in the measured data.

The two-dimensional model plane coincides with the horizontal ground plane, so the model does not intrinsically include the effect of the ground surface. To compare the calculated waveforms with the measured data, the ground is assumed to be rigid (finite ground impedance effects are neglected) and the direct and reflected path lengths equal; these assumptions imply that the calculated model pressures be multiplied by a factor of 2 to account for ground reflection. The factor of 2 is included in the modeling results when compared with the recorded data. This approach is accurate for frequencies up to about 600 Hz, but would have to be modified for higher frequency propagation or for propagation over more porous grounds.

Memory constraints in the 1-GB personal computer used in the calculations limit the problem size to a total of about 1.2 million spatial grid points. With a spatial grid interval of 0.1 m, a two-dimensional problem of 110 m<sup>2</sup> can be studied, compared to a volume of only 10.6 m<sup>3</sup> that could be computed in the full three-dimensional case. The reader should also remain aware that energy outside the plane of the propagation model is ignored, i.e., propagation over the top of a

berm, wall, or building is not included in the model. As the results below will show, this limitation introduces only a surprisingly small error.

### C. Source waveform

The source waveform used for the calculations (Fig. 4) is based on measurement close to the source and is modified from the theoretical blast wave source pulse presented by Reed.<sup>28</sup> The analytical expression for the source pressure as a function of time is

$$p(t) = A(1 - a[ft - b]^2) \exp(-cft), \quad (5)$$

where  $p(t)$  is the source pressure at time  $t$ ,  $A$  is the source strength,  $a$ ,  $b$ , and  $c$  are constants that determine the delay, rise time, and the amplitude of the negative trough of the source waveform, and  $f$  is the central frequency of the pulse. A value for  $f$  of 150 Hz was found to produce a source waveform similar to that measured for the type and size of explosive sources used in this study. When used to construct the starting pulse for the simulations, this frequency value also produced good agreement with the measured waveforms as will be discussed below. Other source waveforms can easily be used in the FDTD simulations if desired.

### D. Material parameters used in the simulations

A sound speed of 353 m s<sup>-1</sup> was measured using a blank pistol as the source of the waves, slightly higher than the expected sound speed of about 350 m s<sup>-1</sup> for the air temperature of about 32 °C. However, for the small explosions a sound speed of 370 m s<sup>-1</sup> was measured. This higher speed is a weak nonlinear effect caused by higher pressures of the blast waves, and corresponds to a Mach number of about 1.05.<sup>29</sup> Thus in the finite difference calculations a sound speed of 370 m s<sup>-1</sup> and a density of 1.2 kg m<sup>-3</sup> are used to represent air, giving an acoustic impedance of 440 kg m<sup>-2</sup> s<sup>-1</sup>.

Concrete has a nominal density of  $2300 \text{ kg m}^{-3}$  and an acoustic wave speed of  $2950 \text{ m s}^{-1}$  for an acoustic impedance of  $6.8 \times 10^6 \text{ kg m}^{-2} \text{ s}^{-1}$ . The very large impedance contrast with air imposes a more strict stability condition than the classic Courant condition<sup>30</sup> so that the final selections of the grid size and time step were determined by the material contrast. However, using realistic values of the material properties for air and concrete makes the simulation unrealistically expensive in both memory and CPU time. To avoid these problems, the impedance contrast must be reduced to a manageable level. In these simulations, the full velocity contrast (a ratio of 1/8) is implemented to capture the correct propagation phenomenology, but the density contrast is limited to about 1/20 instead of the true ratio of 1/2000 by reducing the density of the concrete wall from  $2300 \text{ kg m}^{-3}$  to a value of  $23 \text{ kg m}^{-3}$ . Physically, this change does not affect the arrival times of the waves or the propagation behavior. Using a lower density for concrete reduces the impedance ratio from approximately 15 000 to about 150, and also makes a slight change in the reflection and transmission coefficients. For example, the true normal reflection coefficient value of 0.999 94 will be replaced by a value of 0.989 74, about a 1% change in reflection coefficient.

As shown by Schröder and Scott,<sup>30</sup> a high impedance contrast may introduce numerical instabilities in the finite-difference solution. Three steps have been taken in the calculations presented here to eliminate these instabilities. First, the impedance contrast between air and concrete is reduced by lowering the density of concrete used in the calculations as discussed in the preceding paragraph. This adjustment reduces the impedance ratio from  $15k$  to 150, while the reflection coefficient and wave velocities remain unaffected. Second, following Schröder and Scott,<sup>30</sup> the first grid layer at the air-wall boundary uses the average impedance between air and concrete instead of the full impedance contrast. Finally, the time step is reduced from the classical Courant condition given in Eq. (3) to the much more stringent condition of Eq. (4). Imposing these conditions on the calculations insured their stability and also gave good accuracy, as demonstrated by comparison with field measurements in the following section.

Although rigid boundaries can be used in the simulations, they may introduce complications in the discretization of complex geometries and cause further numerical instability and so were not included in the calculations presented here. The shear properties of the wall are also ignored in these acoustic wave simulations.

### 1. Analytical comparison

To validate the approximations made to reduce the impedance contrast between the concrete walls and air, the analytical reflection coefficient for a planar surface is compared to the reflection coefficient calculated using the FDTD method. A symmetric Ricker wavelet with a frequency of 100 Hz was used in this finite-difference calculation. The analytical reflection coefficient is given by

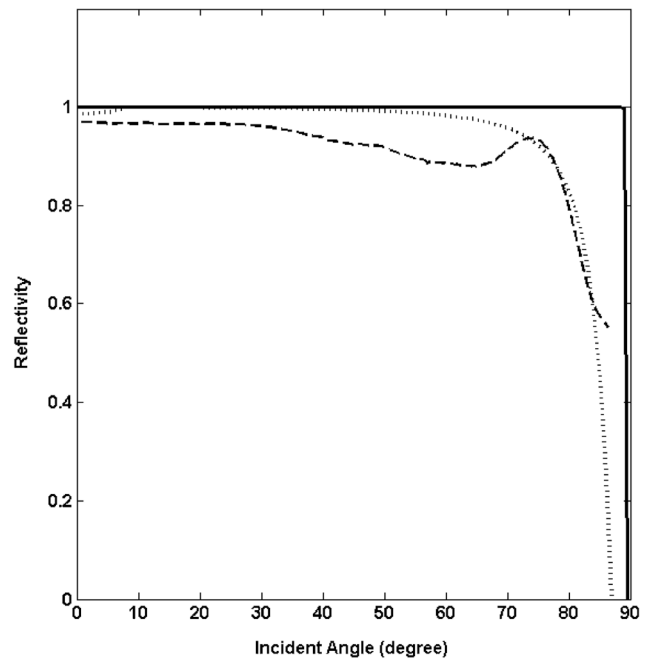


FIG. 5. Comparison of the analytical reflection coefficient with the FDTD reflection coefficient for an air-concrete surface as a function of angle of incidence. The solid line is the analytical result for the true concrete impedance ( $Z=15k$ ) and the dotted line is the analytical result when the concrete density is reduced as discussed in the text. These coefficients were calculated using Eq. (6). The dashed line is the finite difference result for a 100-Hz Ricker wavelet.

$$R = \frac{Z_1 \cos \theta - Z_0 \cos \theta}{Z_1 \cos \theta + Z_0 \cos \theta}, \quad (6)$$

where  $Z_i = \rho_i c_i$  are the concrete and air impedances and  $\theta$  is the angle of incidence (with  $\theta=0$  at normal incidence). Figure 5 compares two analytical reflection coefficients, one with the full impedance contrast and one calculated with a lower concrete density as discussed previously. All of the calculation methods give a reflection coefficient near one for all angles of incidence below  $80^\circ$ . The finite-difference method matches the reduced density concrete coefficient at grazing angles above  $80^\circ$ . This approximation is acceptable for the propagation environment discussed in this paper.

The major advantage of simulating the building effects with a two-dimensional FDTD code is that fewer computational resources are needed compared to a full three-dimensional simulation. For example, each two-dimensional simulation in this paper required about 155 min to complete on a 1.6-GHz personal computer. A substantial part of this time was used to write 250 movie frames for each computation. Because the finite-difference code is written in MATLAB, converting to a compiled language like FORTRAN is likely to provide substantial improvements in the speed of the computations in the future.

## IV. SIMULATION RESULTS FOR A RIGHT-ANGLE WALL

In this section, the finite-difference simulation for the experimental geometry shown in Fig. 1 is discussed and

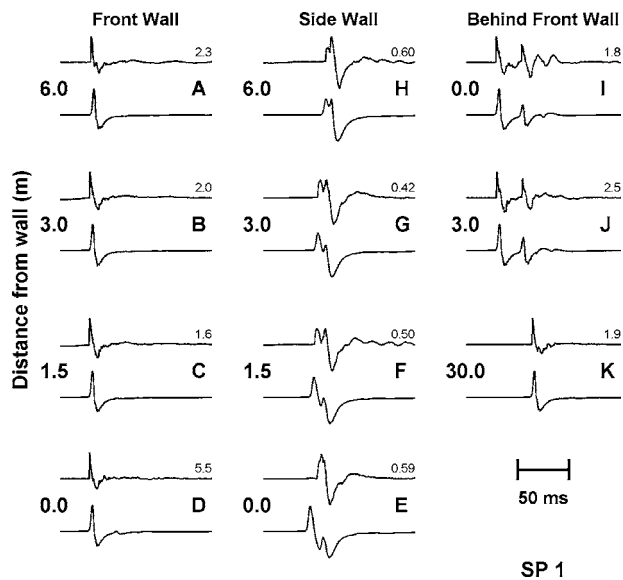


FIG. 6. Comparison of measured and calculated pressure waveforms for the geometry shown in Fig. 1 with the source at SP 1. The left and center columns show waveforms for sensors A–D located near the front wall and sensors E–H located near the side wall. The right column shows the sensors I and J located behind the front wall. For each sensor location, the top trace is the measured signal (with the absolute peak pressure in kPa indicated) and the bottom trace is the calculated signal. Each waveform is 150 ms in duration and has been normalized. (The upper left and bottom center measured waveforms were shown in Fig. 3.)

compared to the measured waveforms. The two-dimensional finite-difference simulation was run separately for sources located in the five source positions (SPs) shown in Fig. 1. For these simulations, a  $600 \times 700$  grid of nodes was used with a spatial sampling of 0.1 m; thus, the simulated area was  $60 \times 70$  m with absorbing boundaries at the edges. The time step was  $16.67 \mu\text{s}$ , and the simulation ran for 15 000 time steps, providing a total time window of 0.25 s.

In the calculations, the concrete wall was assigned a density of  $23 \text{ kg m}^{-3}$  and an acoustic wave speed of  $2950 \text{ m s}^{-1}$ , while the air surrounding the wall was assigned a density of  $1.2 \text{ kg m}^{-3}$  and a sound speed of  $370 \text{ m s}^{-1}$  as discussed earlier. For the frequency band (less than 200 Hz) and propagation distances (less than 100 m) used here, the intrinsic absorption of the atmosphere is negligible and has been ignored in the calculations.

### A. Comparison with measurements in the time domain

Figures 6–10 compare the measured waveforms with the waveforms calculated using the finite-difference method for each source location. For each waveform pair shown in the figures, the upper waveform has been measured experimentally while the lower waveform has been calculated using the two-dimensional FDTD method. The left column of each of these figures shows the sensors (A–D) located near the front wall. These sensors are line-of-sight (LOS) in all cases. The center column of each figure shows the results from the sensors (E–H) located near the side wall, and the right column of each figure shows the results from the sensors (I–K) lo-

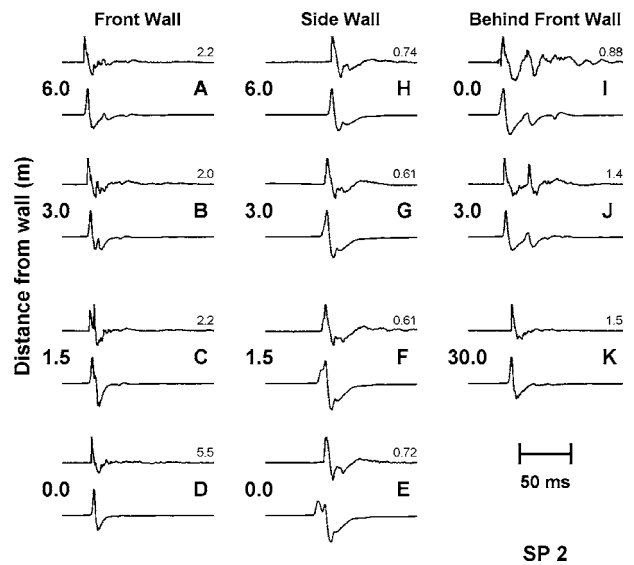


FIG. 7. Comparison of measured and calculated pressure waveforms for the geometry shown in Fig. 1 with the source at SP 2. The left and center columns show waveforms for sensors A–D located near the front wall and sensors E–H located near the side wall. The right column shows the sensors I and J located behind the front wall. For each sensor location, the top trace is the measured signal (with the absolute peak pressure in kPa indicated) and the bottom trace is the calculated signal. Each waveform is 150 ms in duration and has been normalized. The bottom right waveforms for the location 30 m behind the front wall have been advanced by 50 ms for this plot.

cated behind the front wall. Sensors in the center and right columns are sometimes NLOS as discussed previously; see Fig. 1 and Table I.

In Fig. 6 (for SP 1), the source is located at a grazing angle with respect to the front wall, and no reflected waves appear in the measurements or in the simulations. As the

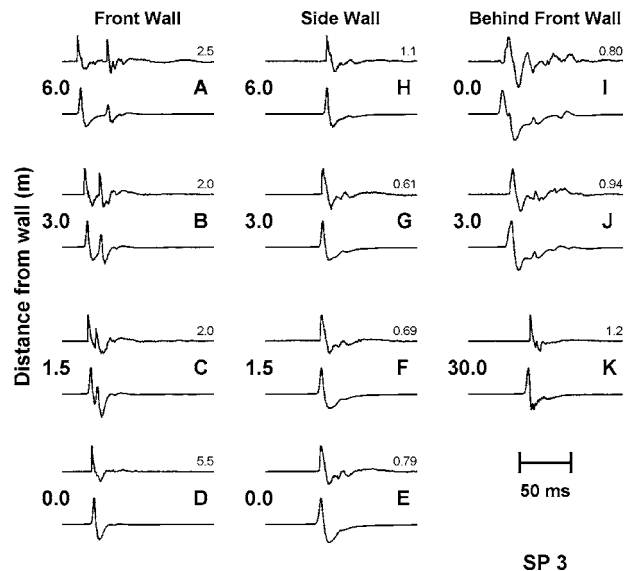


FIG. 8. Comparison of measured and calculated pressure waveforms for the geometry shown in Fig. 1 with the source at SP 3. The left and center columns show waveforms for sensors A–D located near the front wall and sensors E–H located near the side wall. The right column shows the sensors I and J located behind the front wall. For each sensor location, the top trace is the measured signal (with the absolute peak pressure in kPa indicated) and the bottom trace is the calculated signal. Each waveform is 150 ms in duration and has been normalized. The bottom right waveforms for the location 30 m behind the front wall have been advanced by 50 ms for this plot.

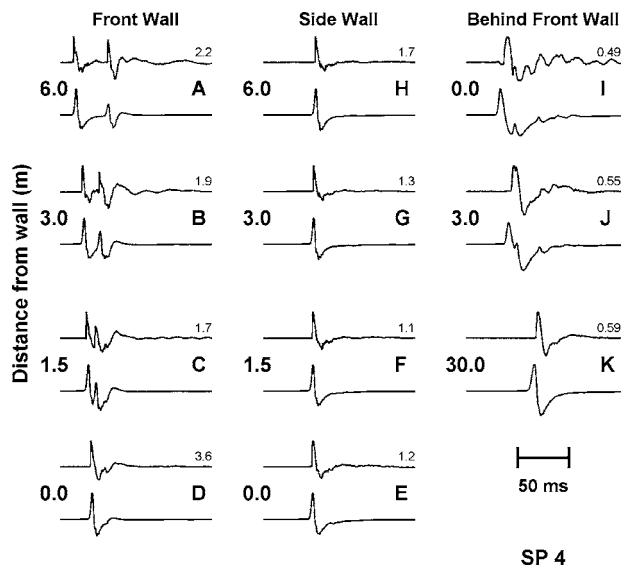


FIG. 9. Comparison of measured and calculated pressure waveforms for the geometry shown in Fig. 1 with the source at SP 4. The left and center columns show waveforms for sensors A–D located near the front wall and sensors E–H located near the side wall. The right column shows the sensors I and J located behind the front wall. For each sensor location, the top trace is the measured signal (with the absolute peak pressure in kPa indicated) and the bottom trace is the calculated signal. Each waveform is 150 ms in duration and has been normalized. The bottom right waveforms for the location 30 m behind the front wall have been advanced by 50 ms for this plot.

source position is moved to produce the following figures, the waveforms in the left column show the reflected wave interfering with the direct wave. In all cases, the agreement between the observed and calculated waveforms is very good.

The center column of Figs. 6–10 shows the waveforms

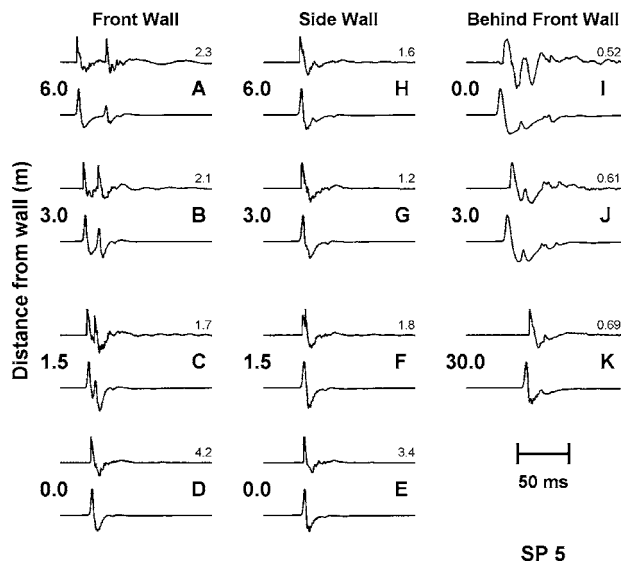


FIG. 10. Comparison of measured and calculated pressure waveforms for the geometry shown in Fig. 1 with the source at SP 5. The left and center columns show waveforms for sensors A–D located near the front wall and sensors E–H located near the side wall. The right column shows the sensors I and J located behind the front wall. For each sensor location, the top trace is the measured signal (with the absolute peak pressure in kPa indicated) and the bottom trace is the calculated signal. Each waveform is 150 ms in duration and has been normalized. The bottom right waveforms for the location 30 m behind the front wall have been advanced by 50 ms for this plot.

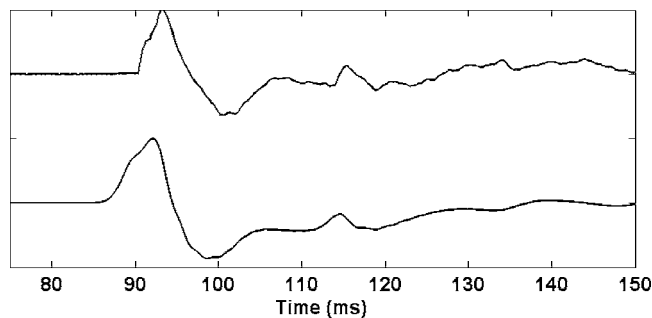


FIG. 11. Comparison of measured and calculated pressure waveforms for sensor J located 3 m behind the front wall and with the source located at SP 3. The top trace is the measured signal and the bottom trace is the FDTD-calculated signal. Each waveform is 75 ms in duration and has been normalized. Based on comparison with the calculated waveform and the wavefront movie (Fig. 12), the arrival at 93 ms is identified as a diffraction around the left edge of the front wall (–9.4, 0), the arrival at 115 ms is this same wave reflected off the rear (the left side in Fig. 1) of the side wall, and the arrival at 135 ms is a diffraction from the bottom corner of the side wall (0.0, –9.4). Refer to Fig. 1 for the wall geometry.

for sensors E–H on the side wall. With the source at SP 1 (Fig. 6), all of these sensors are directly behind the side wall in the deep shadow zone. All of the observed and calculated waveforms have longer durations than the LOS sensors. The waveform agreement is generally good, although there are some visible differences. The observed waveforms often show a second arrival peak that is larger in amplitude than the second arrival in the calculated waveforms. This difference may arise because the calculations are ignoring any diffractions over the top of the wall due to the two-dimensional nature of the model. As the source moves in Figs. 6–10, the diffraction angle decreases and the agreement between the observed and calculated waveforms improves. The transition from NLOS to LOS is accurately depicted in the calculated waveforms.

The right column in Figs. 6–10 compares the sensors (I–K) located behind the front wall. Here, the results for SP 1 (Fig. 6) show direct waves and waves reflected from the left surface of the side wall (Fig. 1) for the first two sensors, while the sensor located 30 m away is unaffected by the wall’s presence. The agreement between the observed and calculated waveforms is very good in this and in subsequent figures. Again, the NLOS waveforms exhibit longer durations and lower amplitudes than the LOS waveforms. The measured waveforms for the sensor located directly on the back of the front wall show more oscillations than the calculated waveforms for this position and more oscillations than any of the other measurements in all cases. This excessive oscillation is believed to be caused by a loose sensor mounting or poor sensor performance (“ringing”). Despite these discrepancies, the main characteristics of the calculated waveforms are visible in the measured waveforms.

## B. Comparison with measurements in the spatial domain

One very useful advantage of the finite-difference method is the ability to save snapshots of the pressure wave field at any time step in the calculation. By assembling such snapshots in sequence, a movie of the wave-field evolution is

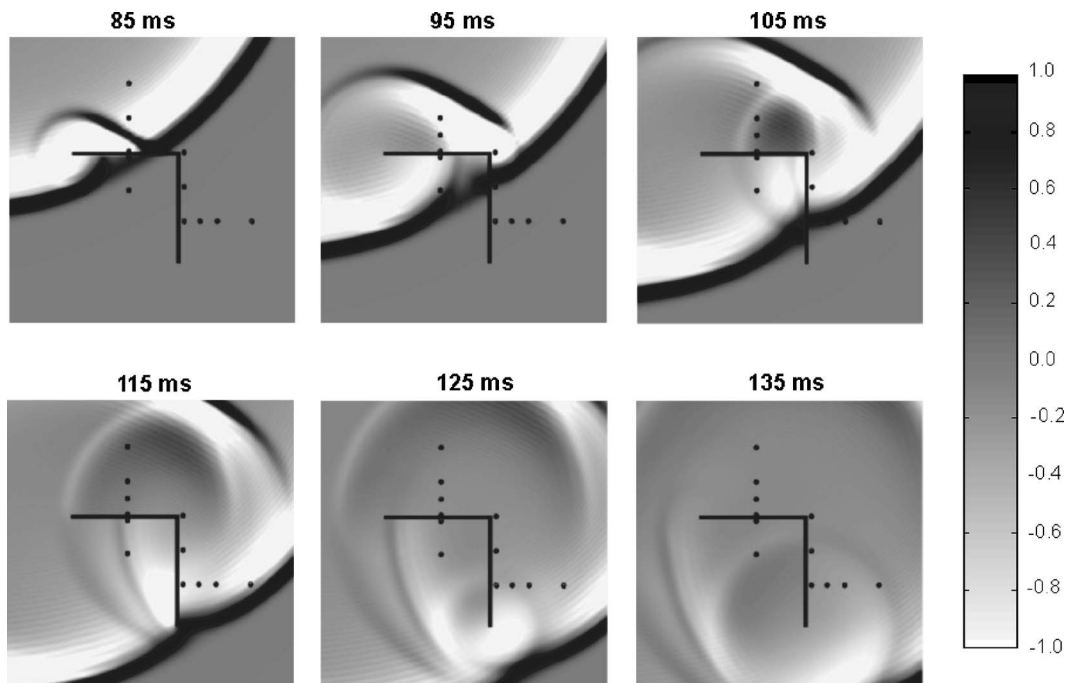


FIG. 12. Snapshots of an acoustic pulse produced by a source at SP 3 interacting with the concrete wall. These movie frames were generated using the finite-difference time domain method discussed in the text.

produced that is very useful for understanding details of the individual sensor waveforms. As an example, the measured and calculated waveforms for sensor J, located 3.0 m behind the front wall, when the source was at SP 3 is shown in Fig. 11. For the measured waveform, aside from the largest arrival at 93 ms, other positive pressure arrivals are visible at 115 and 135 ms. For the calculated waveform, the arrival times are about 91, 112, and 135 ms, respectively.

Figure 12 shows some selected wave-field snapshots for the SP 3 source position. By examining these snapshots and the full movie, we can determine the source of the individual positive arrivals. From Fig. 12, the large first arrival on the sensor 3 m from the back of the front wall is clearly seen to be a wave diffracting around the left corner of the front wall. There is also probably some transmission through the wall. In the measurement, there must also be energy propagating over the top of the wall that is ignored in the calculations.

By following the wave-fronts through a series of snapshots, the arrival at about 115 ms is identified as the reflection of the diffracted wave from the back (left) side of the side wall. Finally, the arrival at 135 ms can be identified as a diffracted wave from the bottom corner of the side wall, a wave that is rarely considered in diffraction problems. Although the pressure amplitudes of these later arrivals are small, their identification through the use of the wave-field snapshots adds to the understanding of the acoustic wave interaction with the wall. The ability to identify and elucidate wave arrivals may be especially helpful in situations with more complicated geometries, for example when full four-sided or multiple buildings are present.

## V. CONCLUSIONS

Measurements of acoustic pulse propagation near a concrete right-angle wall were presented in this paper. The mea-

surements confirm that diffraction acts like a strong low-pass filter, greatly reducing frequencies above 100 Hz and reducing the peak amplitude by a factor of about  $\frac{1}{4}$ .

The finite-difference method was used to calculate theoretical waveforms for comparison with the experimental measurements. Using a simplified two-dimensional representation of the wall gave fast computation times and good agreement with measured arrival times, peak amplitudes, and waveform characteristics for which no analytical techniques exist. This simulation method can be used to investigate propagation in more complicated multiple building urban environments. The comparison shows that the limitation to a two-dimensional geometry speeds up the calculations significantly while introducing only small errors in accuracy.

## ACKNOWLEDGMENTS

We thank, Rich Andrejkovics, SYDET Project Officer, PM-CCS, for funding the experimental work, and the US Army Corps of Engineers Engineering Research and Development Center for funding the analysis. Michael Scanlon, Army Research Laboratory, assisted in the design of the single wall experiment, and Bill Davis, Aberdeen Test Center, safely and efficiently handled the work with the explosives. We also thank the many people who assisted with the field measurements, including Steve Decato, Dave Carbee, and Dr. Joyce Nagle of ERDC-CRREL, and Chris Reiff and Dave Gonski of ARL. Finally, we greatly appreciate the helpful comments of the Associate Editor, Lou Sutherland, and two anonymous reviewers.

## APPENDIX: YEE (1966) ALGORITHM USING STAGGERED GRID AND LEAPFROG TIME-STEPPING

The method proposed by Yee<sup>20</sup> to solve the Maxwell equations for electromagnetic wave propagation uses a leap-

frog scheme on staggered Cartesian grids. This method can be applied to acoustic problems<sup>23,24</sup> using the first-order, velocity-pressure coupled differential equations:

$$\begin{aligned} \frac{\partial p}{\partial x} &= -\rho \frac{\partial u}{\partial t}, \\ \frac{\partial p}{\partial y} &= -\rho \frac{\partial v}{\partial t}, \\ \frac{\partial u}{\partial x} + \frac{\partial v}{\partial y} &= -\frac{1}{\rho c^2} \frac{\partial p}{\partial t}, \end{aligned} \quad (\text{A1})$$

where  $u$  and  $v$  are the  $x$  and  $y$  components of the particle velocity,  $p$  is the pressure,  $\rho$  is the density, and  $c$  is the sound speed of the medium. [These are Eqs. (1)-(3) of Ref. 24 and Eq. (1) of this text.] For a spatial grid size of  $h$ , the first-order spatial partial derivatives appearing in the above equations can be approximated by

$$\frac{\partial u}{\partial x} \Big|_{t=n\Delta t} \approx \frac{1}{2h} [u(i+1, j; n) - u(i-1, j; n)] \quad (\text{A2})$$

with similar approximations for the  $y$  and  $t$  derivatives. In the above equation,  $u(i, j; n)$  represents the  $x$  component of the particle velocity at  $(x, y)$  grid point  $(i, j)$  and at time step  $n$ . Following Yee's approach and using the approximation in (A2) the equations of motion can be solved in finite-difference form [see Eqs. (7)–(9) in Ref. 24]:

$$\begin{aligned} u_{i+1/2, j}^{n+1/2} &= u_{i+1/2, j}^{n-1/2} - \frac{\Delta t}{\rho_{i, j} \Delta x} (p_{i+1, j}^n - p_{i, j}^n), \\ v_{i+1/2, j}^{n+1/2} &= v_{i+1/2, j}^{n-1/2} - \frac{\Delta t}{\rho_{i, j} \Delta y} (p_{i, j+1}^n - p_{i, j}^n), \end{aligned} \quad (\text{A3})$$

$$p_{i, j}^{n+1} = p_{i, j}^n - \Delta t \rho_{i, j} c^2 \left( \frac{u_{i+1/2, j}^{n+1/2} - u_{i-1/2, j}^{n+1/2}}{\Delta x} + \frac{v_{i, j+1/2}^{n+1/2} - v_{i, j-1/2}^{n+1/2}}{\Delta y} \right).$$

The staggered Cartesian grid used in Eq. (A3) is sketched in Fig. 13. Equations (A3) show how updated values of pressure and particle velocity are obtained from previous values on the staggered grid.

The Yee algorithm is robust, fast, and simple to understand and has several properties and advantages that differ from some other numerical finite-difference methods. First, the Yee method simultaneously solves two coupled physical fields (pressure and particle velocities in acoustics) through a set of first-order partial differential equations, instead of solving for a single, second-order partial differential equation for one of the two physical fields. This solution algorithm is more robust than solving either field alone.

Second, the algorithm is very flexible in taking advantage of specific features unique to each field, such as acoustically hard (particle velocity assigned to be zero) or acoustically soft (pressure to be zero) regions. Third, the finite-difference expressions for spatial derivatives are central difference in nature and second-order accurate.

Fourth, the leapfrog time-stepping used is also central difference in nature and second-order accurate. Since this

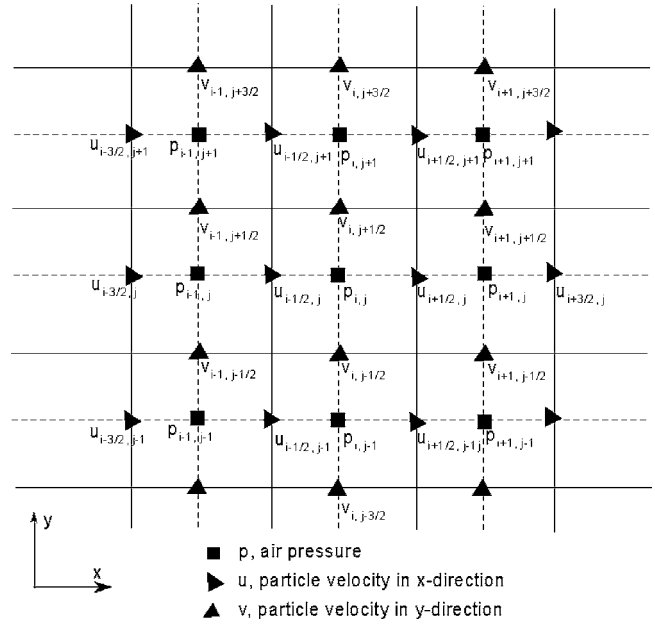


FIG. 13. A sketch of the two-dimensional staggered grid system in the  $x$ - $y$  plane used by the finite-difference method for simulation of the acoustic field. The index  $i$  is used to indicate  $x$  coordinates, and the index  $j$  to indicate  $y$  coordinates.

approach is fully explicit, it avoids problems involved with simultaneous equations and matrix inversion. Finally, the method can be used to determine the response in a chosen frequency band in one calculation by using a pulse excitation. This cannot be achieved with frequency domain methods.

The disadvantages of the Yee algorithm are those shared by all finite-difference approaches. If the Cartesian grid does not conform well to the real geometry of a particular problem, so called "stair stepping" errors will be introduced. In addition, the absence of a general subgridding scheme means that structures smaller than the resolution have to be treated by subcell models. These models are currently limited to relatively simple geometrical structures such as wires, gaps, layers, etc., and introduce additional complexity to the calculations.

<sup>1</sup>D. R. Raichel, *The Science and Applications of Acoustics* (Springer-Verlag, New York, 2000).

<sup>2</sup>E. M. Salomons, *Computational Atmospheric Acoustics* (Kluwer Academic, Dordrecht, 2001).

<sup>3</sup>A. D. Pierce, "Diffraction of sound around corners and over wide barriers," *J. Acoust. Soc. Am.* **55**, 941–955 (1974).

<sup>4</sup>A. D. Pierce, *Acoustics. An Introduction to its Physical Principles and Applications* (Acoustical Society of America, Woodbury, NY, 1989).

<sup>5</sup>D. C. Hothersall, S. N. Chandler-Wilde, and M. N. Hajmizae, "Efficiency of single noise barriers," *J. Sound Vib.* **146**, 303–322 (1991).

<sup>6</sup>S. N. Chandler-Wilde, "The boundary element method in outdoor noise propagation," *Proc. Inst. Acoust.* **19** (Part 8), 27–50 (1997).

<sup>7</sup>T. W. Wu, ed., *Boundary Element Acoustics: Fundamentals and Computer Codes* (WIT, Boston, 2000).

<sup>8</sup>J. Kang, "Sound propagation in street canyons: Comparison between diffusively and geometrically reflecting boundaries," *J. Acoust. Soc. Am.* **107**, 1394–1404 (2000).

<sup>9</sup>J. Picaut, L. Simon, and J. Hardy, "Sound field modeling in streets with a diffusion equation," *J. Acoust. Soc. Am.* **106**, 2638–2645 (1999).

<sup>10</sup>K. K. Lu and K. M. Li, "The propagation of sound in narrow street canyons," *J. Acoust. Soc. Am.* **112**, 537–550 (2002).

<sup>11</sup>C. G. Don, "Application of hard truncated wedge theory of diffraction to

- wide barriers," *J. Acoust. Soc. Am.* **90**, 1005–1010 (1991).
- <sup>12</sup>A. I. Papadopoulos and C. G. Don, "A study of barrier attenuation by using acoustic impulses," *J. Acoust. Soc. Am.* **90**, 1011–1018 (1991).
- <sup>13</sup>D. J. Saunders and R. D. Ford, "A study of the reduction of explosive impulses by finite sized barriers," *J. Acoust. Soc. Am.* **94**, 2859–2875 (1993).
- <sup>14</sup>R. Raspet, J. Ezell, and S. V. Coggshall, "Diffraction of an explosive transient," *J. Acoust. Soc. Am.* **79**, 1326–1334 (1986).
- <sup>15</sup>H. Medwin, E. Childs, and G. M. Jebsen, "Impulse studies of double diffraction: a discrete Huygens interpretation," *J. Acoust. Soc. Am.* **72**, 1005–1013 (1982).
- <sup>16</sup>K. B. Rasmussen, "Model experiments related to outdoor propagation over an earth berm," *J. Acoust. Soc. Am.* **96**, 3617–3620 (1994).
- <sup>17</sup>X. Yuan, D. Borup, J. W. Wiskin, M. Berggren, R. Eidens, and S. A. Johnson, "Formulation and validation of Berenger's PML absorbing boundary for the FDTD simulation of acoustic scattering," *IEEE Trans. Ultrason. Ferroelectr. Freq. Control* **44**, 816–822 (1997).
- <sup>18</sup>H. Dong, A. M. Kaynia, C. Madshus, and J. M. Hovem, "Sound propagation over layered poro-elastic ground using a finite-difference model," *J. Acoust. Soc. Am.* **108**, 494–502 (2000).
- <sup>19</sup>A. Taflove and S. C. Hagness, *Computational Electromagnetics* (Artech House, Boston, 2000).
- <sup>20</sup>K. S. Yee, "Numerical solution of initial boundary value problems involving Maxwell's equations in isotropic media," *IEEE Trans. Antennas Propag.* **14**, 302–307 (1966).
- <sup>21</sup>R. A. Stephen, "A review of finite difference methods for seismo-acoustics problems at the seafloor," *Rev. Geophys.* **26**, 445–458 (1988).
- <sup>22</sup>F. B. Jensen, W. A. Kuperman, M. B. Porter, and H. Schmidt, *Computational Ocean Acoustics* (American Institute of Physics, New York, 1994).
- <sup>23</sup>J. Virieux, "SH-wave propagation in heterogeneous media: Velocity-stress finite difference method," *Geophysics* **49**, 1933–1942 (1984).
- <sup>24</sup>S. Wang, "Finite-difference time-domain approach to underwater acoustic scattering problems," *J. Acoust. Soc. Am.* **99**, 1924–1931 (1996).
- <sup>25</sup>J. P. Berenger, "A perfectly matched layer for the absorption of electromagnetic waves," *J. Comput. Phys.* **114**, 185–200 (1994).
- <sup>26</sup>G. Festa and S. Nielsen, "PML absorbing boundaries," *Bull. Seismol. Soc. Am.* **93**, 891–903 (2003).
- <sup>27</sup>L. Liu and S. A. Arcone, "Numerical simulation of the wave-guide effect of the near-surface thin layer on radar wave propagation," *J. Environ. Eng. Geophys.* **8**, 133–141 (2003).
- <sup>28</sup>J. W. Reed, "Atmospheric attenuation of explosion waves," *J. Acoust. Soc. Am.* **61**, 39–47 (1977).
- <sup>29</sup>G. F. Kinney and K. J. Graham, *Explosive Shocks in Air* (Springer-Verlag, Berlin, 1985).
- <sup>30</sup>C. T. Schroder and W. R. Scott, "On the stability of the FDTD algorithm for elastic media at a material interface," *IEEE Trans. Geosci. Remote Sens.* **40**, 474–481 (2002).